A wash-free ER marker to monitor micropolarity during ER stress and visualize ER-Golgi transport

Tanoy Dutta,[a] Aditya Nigam,[b] Shilpi Minocha,[b] and Apurba Lal Koner*[a]*

T. Dutta, A. L. Koner
Bionanotechnology Laboratory, Department of Chemistry, Indian Institute of Science Education and Research Bhopal, Bhopal Bypass Road, Bhopal- 462066, INDIA
E-mail: tanoy16@iiserb.ac.in, akoner@iiserb.ac.in

A. Nigam, S. Minocha
Kusuma School of Biological Sciences, Indian Institute of Technology Delhi, Hauz Khas, New Delhi - 110016, INDIA

Keywords: nitrobenzoxadiazole dyes, ER stress, ER to Golgi transport, organelle communication

Cellular stress plays a key role to regulate and maintain organismal as well as microenvironmental homeostasis. The stress-induced response is also reflected in the micropolarity of any specific cellular compartment which is essential to be quantified for early disease diagnosis. Alongside, coming up with a biocompatible small-molecule fluorophore **NBD-Oct** for exclusive endoplasmic reticulum (ER) localization simply driven by its hydrophobicity, in this contribution we present a quantitative study of micropolarity alteration inside the ER during G_1/S and G_2/M phases. The cell cycle arrests caused by the induced ER stress led to the enhancement of the ER micropolarity in cells. **NBD-Oct** is selected among a series of analogous probes based on its fastest diffusion properties demonstrated by fluorescence recovery after photobleaching experiment. The probe is a versatile staining agent as it could efficiently stain the ER in live/fixed mammalian cells, isolated ER, *Caenorhabditis elegans*, and mice tissues. Finally, a well-known biological event, ER to Golgi transport is also visualized by live-cell fluorescence microscopy using this probe. We believe our exhaustive investigation of micropolarity using NBD-based dye provides a new avenue to study ER stress that may unravel a deeper understanding of proteostasis in model systems and potentially even fixed patient samples.

1. Introduction

The endoplasmic reticulum (ER) is one of the most important and largest multifunctional organelles present in eukaryotic cells associated with the synthesis and transport of secretaries as well as membrane proteins, their folding, and lipid metabolism.[1] The post-translational modification along with the glycosylation of proteins is also regulated by ER.[2] The diverse role of ER also includes the regulation of cytosolic calcium levels and carbohydrate metabolism.[3] The ER also undergoes cell cycle-dependent morphological transformations.[4] In the mammalian cell, the usual polygonal network-like structure of the ER becomes much more partitioned and fragmented during cell division. However, such ER morphogenesis during cell cycles is also specific to each cell line.[5] The cell cycle is a combination of biochemical events that result in the accurate duplication of cellular components into genetically identical daughter cells.[6] In the eukaryotic cell, the Synthesis phase or S-phase involves DNA replication while segregation of genetic materials occurs in the Mitosis phase or M-phase. These phases are separated by two gap phases − G_1 and G_2, assigned to protein synthesis, cellular growth, and cell division preparation. Now, while this discussion is aimed to provide a basic idea of the cell cycle process, it is also important to take note of the fact that these complex biochemical processes would have an impact on the micropolarity of the ER. The cell cycle arrest, induced by small molecule drugs, is also associated with unfolded protein response, commonly known as ER stress.[7] The unsettlement of homeostasis due to the accumulation of the misfolded and unfolded proteins in ER during the cell cycle arrest leads to several fatal symptoms and diseases like neurodegeneration, cardiovascular aberration, diabetes, and cancer.[8] On that account, the micropolarity inside ER is expected to be a fundamental physical parameter for monitoring cellular health.[9]

The interaction between ER and Golgi bodies is another well-established intracellular phenomenon − this transport being the primary step in the secretory pathway.[10] The transport mechanism between these two organelles is particularly operated by COP II (coat protein complex II) and COP I-coated transport vesicles.[11] The newly synthesized proteins are exported from ER to Golgi while recycled proteins are sent back from *cis*-Golgi to ER.[12] A handful of studies have been reported to show this transport phenomenon in yeasts and mammalian cells.[13] Sophisticated experimental procedures and expertise are one of the main criteria to perform such kind of experiment. Nevertheless, the current literature is yet to have a report with a small molecule fluorescent reporter as a chemical tool to visualize this phenomenon using optical microscopy. The literature has been enriched with reports

demonstrating several small-molecule ER-targeting fluorescent probes for measuring micropolarity in live cells and animal models.[14] Unfortunately, the quantified approach is missing in most of the cases, and no report mentions how micropolarity changes in G_1 and G_2 cell cycle arrest phases by induced ER stress.

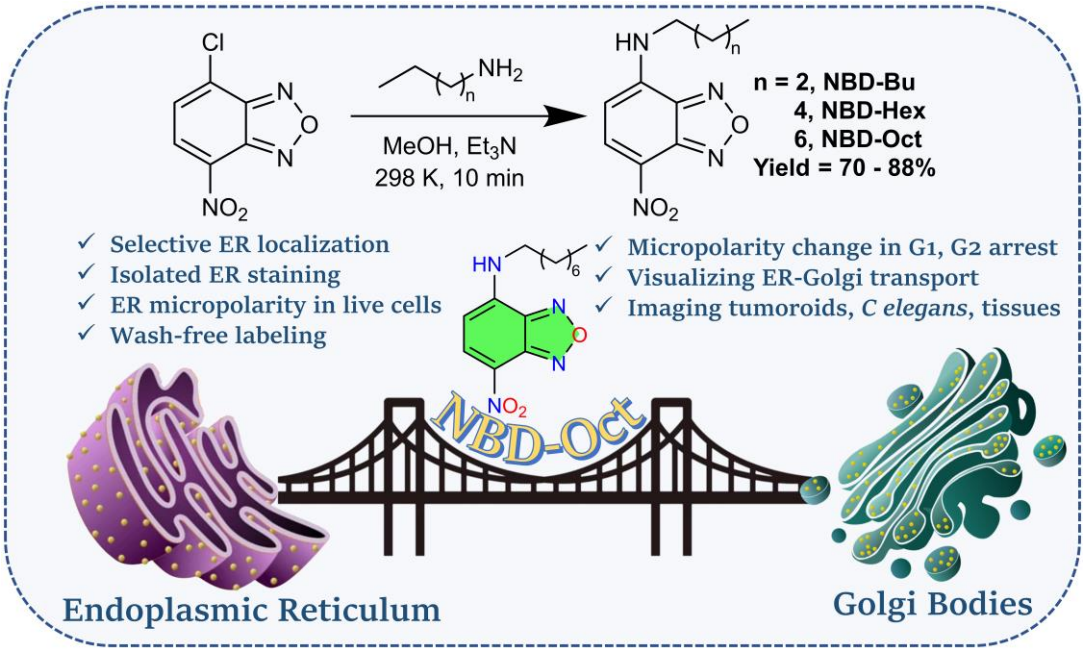

Scheme 1. (above) Synthetic route of the alkylated-NBD probes; (below) schematic representation of the brief overview of this work shows several applications using the probe **NBD-Oct**.

In this contribution, we present a series of three alkylated nitrobenzoxadiazole-based fluorescent probes, developed by straightforward synthetic procedures, manifesting excellent environment sensitivity and exclusive ER targeting abilities. We further judiciously selected **NBD-Oct** among the three probes gleaned from their efficiency of ER localization and diffusion properties by fluorescence recovery after photobleaching experiment. The specificity of the ER labeling of **NBD-Oct** was also validated in isolated ER obtained from subcellular fractionation. Moreover, the fluorescent turn-on feature of these probes, moving from polar to non-polar media, was employed to perform wash-free organelle labeling. Wash-free bioimaging of live cells and tissues is a matter of increasing interest thanks to its simplified analytical procedure and significantly faster detection time while the washing step is practically non-feasible in the case of in vivo imaging.[15] Therefore, developing a wash-free imaging technique using a small organic fluorophore is highly desirable.

Moving forward, the micropolarity of the ER was quantified in several cancerous and non-cancerous cell lines in homeostatic conditions as well as G_1/S and G_2/M cell cycle arrest phases. The stress-induced ER micropolarity was found to be significantly higher as compared to homeostasis. Additionally, the long-term imaging of ER stained with **NBD-Oct** led us to visualize another interesting phenomenon – ER to Golgi transport. Pearson's correlation coefficients, measured with commercially available ER and Golgi trackers at different times, suggested a reduction in exclusive ER localization and allocation in both ER and Golgi. Finally, we have demonstrated **NBD-Oct** to be useful for staining 3D tumoroids, *Caenorhabditis elegans*, and mice tissue sections.

2. Results and Discussion

2.1. Synthesis and spectroscopic characterization of tailored alkylated-NBD dyes

Solvatochromic organelle targeting fluorescent probes are always been a popular choice for monitoring intracellular polarity in homeostatic, stress-induced, and apoptotic conditions.[16] Substituted nitrobenzoxadiazole (NBD) fluorescent probes exhibit excellent sensitivity to solvent polarity, large Stokes shift, and appreciable cellular uptake efficiency.[17] Hence, we have synthesized a series of NBD-based fluoroprobes with varying alkyl chain lengths in order to have enhanced hydrophobicity. An interesting point of concern can be the choice of chain length for these synthesized NBD derivatives. We have considered a few key aspects here *i.e.*, cellular uptakability, photostability, and water solubility. Even though the longer alkyl chains account for enhanced hydrophobicity, the water solubility and cellular uptakability due to bigger size would take a hit. As our ultimate goal was to use these probes for bioimaging applications, we did not opt for longer alkyl chains beyond C8. The synthetic procedure, reported in previous literature, required either elevated temperature or longer reaction times.[18] We present here a significantly faster synthesis time of 10 min at 298 K with high yields (70 - 88%) (**Scheme 1**). The rate of the substitution reaction was impacted by the addition of triethylamine to the reaction medium which enhanced the nucleophilicity of the alkyl amines. The three probes, NBD-Bu, NBD-Hex, and **NBD-Oct** were well characterized by ^{1}H NMR, ^{13}C NMR, and mass spectrometry (**Figure S1-S9**). Furthermore, the exact overlap of their absorption spectra and

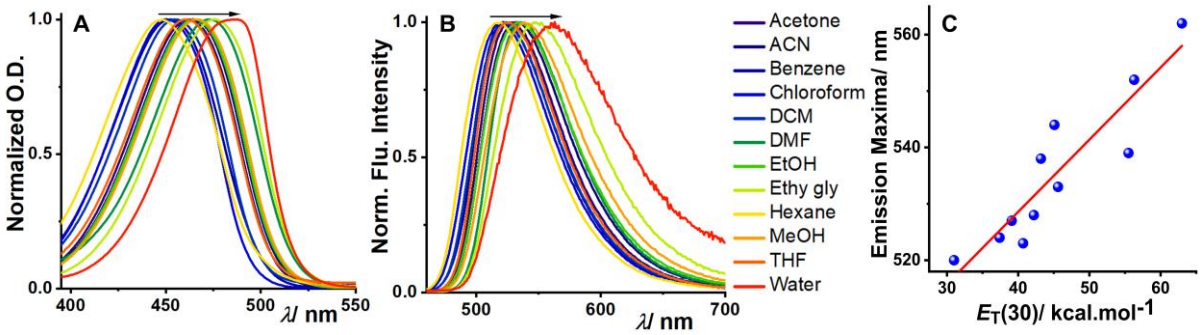

Figure 1. Solvent-dependent (A) UV-Visible and (B) emission spectra of alkylated-NBD probes in different polar solvents, (C) the linear variation (R^2 = 0.92) of the emission maxima of alkylated-NBD probes (5 μM) with the solvent polarity parameter (E_T(30)).

excitation spectra monitored at different wavelengths confirmed the spectroscopic purities of these probes (**Figure S10**). The probes consist of a π-conjugated linker that connects the electron-rich secondary amine (-NH-) moiety with the electron-deficient nitro (-NO_2) group. The electron-rich nitrogen atom is attached to the alkyl chains of varying lengths. The structures of these probes are perfect for exhibiting intra-molecular charge transfer (ICT) behavior thereby showing solvent polarity-dependent photophysical properties (**Table S1–S3**). The absorption and emission spectra of all three probes were recorded in solvents with varying polarity. As per our anticipation, the probes show gradual redshift with increasing polarity, both in the ground and excited states (**Figure 1A-B).** The emission maxima versus solvent polarity parameter, E_T(30) yielded a linear plot suggesting these probes to be sensitive to the environmental polarity (**Figure 1C**). Therefore, we further moved on to our subsequent exploration of live-cell imaging and quantification of intracellular micropolarity using these probes.

2.2. Intracellular localization of the alkylated-NBD dyes

Based on our design principle of the alkylated-NBD probes and inspired by their environment-sensing abilities, we turned to study intracellular localization. Prior to that, the cytotoxic effect of the probes, if any, was monitored using standard MTT [3-(4,5-dimethylthiazole-2-yl)-2,5-diphenyltetrazolium bromide] assay in BHK-21 (baby hamster kidney cells), A549 (human lung cancer cells), MDA-MB-231 (human breast cancer cells), and HeLa (human cervical cancer cells) cell lines for 24 h. The half-maximal inhibitory concentrations, *i.e.*, IC_{50} values in all cell lines were calculated to be around 20 μM (**Figure S11**). Therefore, to perform all the live-cell imaging experiments, 2 μM of the probe concentration was used keeping ~ 80 – 90 % of cells viable, and hence these probes are safe to be termed biocompatible. The optimal

incubation time for efficient cellular uptake was also determined by imaging cells with varying treatment times with the probes and a 10 min incubation period was found to be sufficient for this purpose. Once these experiments provided us with a basic yet foremost understanding of the probes' properties, we moved on to fluorescence colocalization microscopy looking for the specific compartmentalization in live cells. BHK-21 cells were incubated with all three alkylated-NBD probes for 10 min and imaged under a confocal microscope. In the FITC channel, beautiful inter-connected micro-networks were visualized all over the cellular structure except the nucleus (**Figure S12**). We reckoned these to be endoplasmic reticulum (ER) and therefore co-stained the cells with commercial ER labeling dye – ER Tracker Red (**Figure 2A-C**). Pearson's colocalization coefficient (PCC), even though above 0.8 for all (**Figure S13**), was highest for **NBD-Oct** (0.96) having the longest alkyl chain among all three (**Figure 2D**). It is to be noted that all the PCC values were calculated considering the whole frame (whole field of view) and not any single cell.

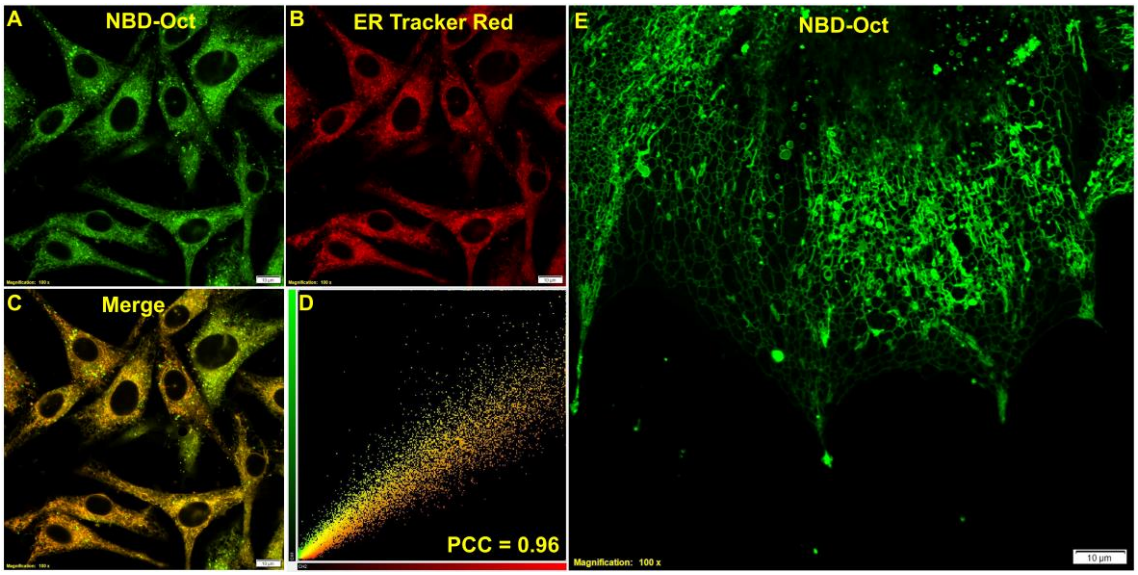

Figure 2. Investigation of subcellular localization of **NBD-Oct** in live BHK-21 cells using fluorescence colocalization microscopy; stained with (A) 2.0 μM of **NBD-Oct** (B) 0.3 μM of ER-Tracker Red (C) merge image of (A) and (B), (D) corresponding scatter plot with Pearson's correlation co-efficient 0.94 ± 0.02 (scale bar: 10 μm); (E) extended ER network in a single cell visualized using 100X objective lens [$\lambda_{ex}/\lambda_{em}$ = 488 nm/500 – 540 nm, laser power: 0.2 %; $\lambda_{ex}/\lambda_{em}$ = 561 nm/575 – 620 nm, laser power: 0.5 %; dwell time: 8 μs/pixel, confocal aperture: 1 AU].

Now, it is well demonstrated that all three probes are efficient ER markers while **NBD-Oct** came up with the best results. The large inter-connected tubular ER network structure of a single cell could be visualized by **NBD-Oct** staining (**Figure 2E**). Furthermore, to confirm the specificity for the ER, the colocalization with other organelle markers *i.e.*, Mito Tracker Red, LysoTracker Red, and LipidSpot were performed which yielded much lower PCC values of 0.43, 0.41, and 0.36 for respective cases (**Figure S14**). As such lipophilic probes are known to have strong hydrophobic interaction with lipid bilayers,[19] we suppose that the alkylated NBD probes bind to the phospholipid bilayer of the ER membrane. The rapid internalization (within a minute) in live cells of the longest chain congener **NBD-Oct** was also demonstrated by time-lapse imaging (**Figure S15**). A quantified approach to understanding the relationship between the length of the side chain and the cellular uptakability of the probes can be obtained from their respective clog P values using the DataWarrior program.[20] The clog P values **NBD-Bu** and NBD-Hex are 1.65 and 2.55 while **NBD-Oct** has a comparatively higher clog P value of 3.47. Now, even though a higher clog P accounts for greater affinity to the lipid phase, the cell permeability is eventually affected. For example, the commercial ER Tracker has a clog P value of 6.79 and it takes a minimum of 20 minutes to label the ER. Therefore, the length of the alkyl chain definitely plays a role to balance lipophilicity and cell permeability.

2.3. Understanding dynamics using Fluorescence recovery after photobleaching (FRAP)

A few studies have shown that probes containing only hydrophobic moiety tethered to the fluorescent reporter, devoid of any specific targeting group, have the propensity to localize in the ER.[21] As demonstrated in our previous experiments, the synthesized alkylated-NBD dyes are not exceptional in this aspect as their localization in ER has been well represented by the colocalization experiments. However, a detailed study of living cells often requires long-term imaging involving continuous exposure to excitation laser sources. Photobleaching is one of the commonest phenomena that limit the use of a fluorophore for such a purpose.[22] Fluorescence recovery after the photobleaching (FRAP) experiment is a useful technique to judge the suitability of a probe to image in living cells for a longer period.[23] This method is also followed to understand the mobility of the labeling dye and analyze the diffusion properties, and spatial distribution in a specific region of a cell or tissue sample. As the set of synthesized molecules has different chain lengths, we anticipated them to exhibit distinct diffusibility after cellular uptake, and the FRAP experiment was performed in live BHK-21 cells (**Figure 3A-F**). The imaging parameters including scanning speed and area, bleaching duration, laser power,

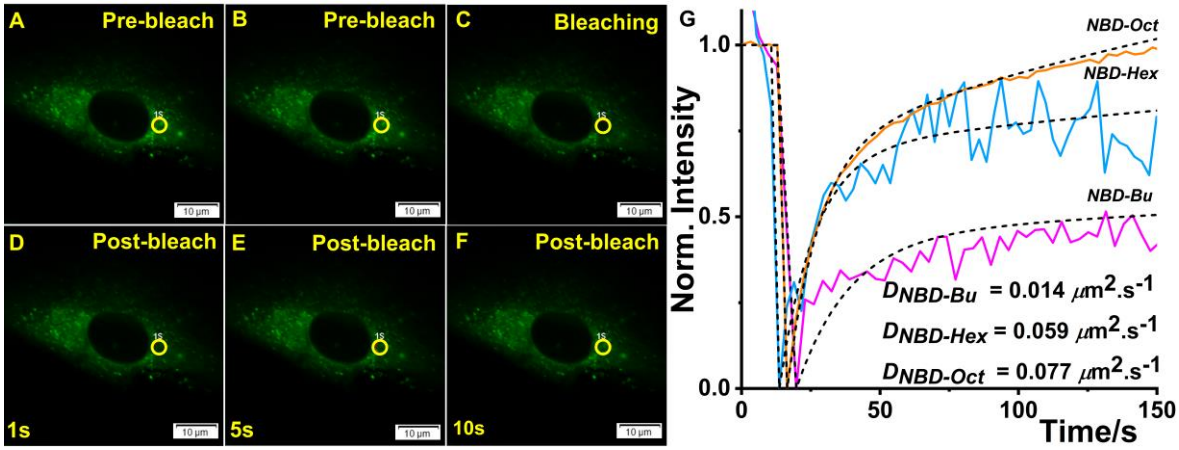

Figure 3. Fluorescence recovery after photobleaching measurement performed in BHK-21 cell line stained with 2 μM **NBD-Oct**. The results show the bleaching and recovery phenomena and the superiority of the **NBD-Oct** derivative compared to the other two. The circular region (1S) represents the bleached region (A) and (B) pre-bleach cycle, (C) bleaching, (D), (E), and (F) shows the recovery of fluorescence after 1s, 5s, and 10s post-bleaching, respectively, (G) the FRAP curve showing the comparative results with all the alkylated-NBD derivatives [$\lambda_{ex}/\lambda_{em}$ = 488 nm/500 – 540 nm, imaging laser power: 0.2 %, bleaching laser power: 5 %, bleaching duration: 2 s, dwell time: 8 μs/pixel, confocal aperture: 1 AU].

and stimulation duration were optimized to avoid any consequential photobleaching in the area of interest. The obtained FRAP data were fitted and analyzed using the Soumpasis equation,[24]

$$\text{Diffusion coefficient, } D_{r_n} = 0.224 \frac{r_n^2}{\tau_{1/2}} \quad (1)$$

where, r_n= radius of the uniformly bleaching spot or sampling region radius, $\tau_{1/2}$= half-time for recovery. The diffusion during photobleaching is assumed to be negligible. Now, from the FRAP analysis, the diffusion coefficient was calculated to be highest for **NBD-Oct** followed by its lower congeners (**Figure 3G**). Hence, **NBD-Oct** is the superior one for bioimaging applications owing to its fastest dynamics and recovery time compared to **NBD-Hex** and **NBD-Bu**. The photostability of **NBD-Oct** in the imaging condition was also examined by the time-lapse imaging in live cells and found that only 10% of photobleaching occurred over the time course (**Figure S16**). More importantly, **NBD-Oct** was less susceptible to being photobleached as compared to both ER Tracker Green and ER Tracker Red (**Figure S17-S18**). Henceforth, considering the colocalization microscopy results, FRAP analysis, and photostability in the biological system we have performed all the imaging experiments on live cells and animal models with **NBD-Oct** only.

2.4. Staining isolated ER, fixed cells, and wash-free imaging

Sub-cellular fractionation and separation have gained popularity for studying specific intra-cellular structures, trafficking, and functions of low-abundance proteins.[25] Even after the separation of the organelles, most of their original biochemical properties are retained. Hence, a biocompatible and photostable small organic fluorescent probe that can stain the isolated ER would attract researchers. Therefore, once the exclusive and efficacious ER staining potency of **NBD-Oct** in live cells was thoroughly validated, we were interested in the possibility of staining the isolated ER using our probe. The subcellular fractionation was performed using live BHK-21 cells and the details procedure has been provided in the supporting information (**Scheme S1**). Briefly, live BHK-21 cells were lysed and centrifuged at 3000 rpm to pellet down nuclei. The supernatant was further centrifuged at 12,000 rpm to remove heavier organelles i.e., mitochondria, lysosomes, endosomes, and any remaining nuclei. Finally, membrane buffer was added to the supernatant, and ultra-centrifugation @70,000 gave the pellet of isolated ER. Now, for imaging purposes, ER pellet was resuspended in membrane buffer followed by co-staining

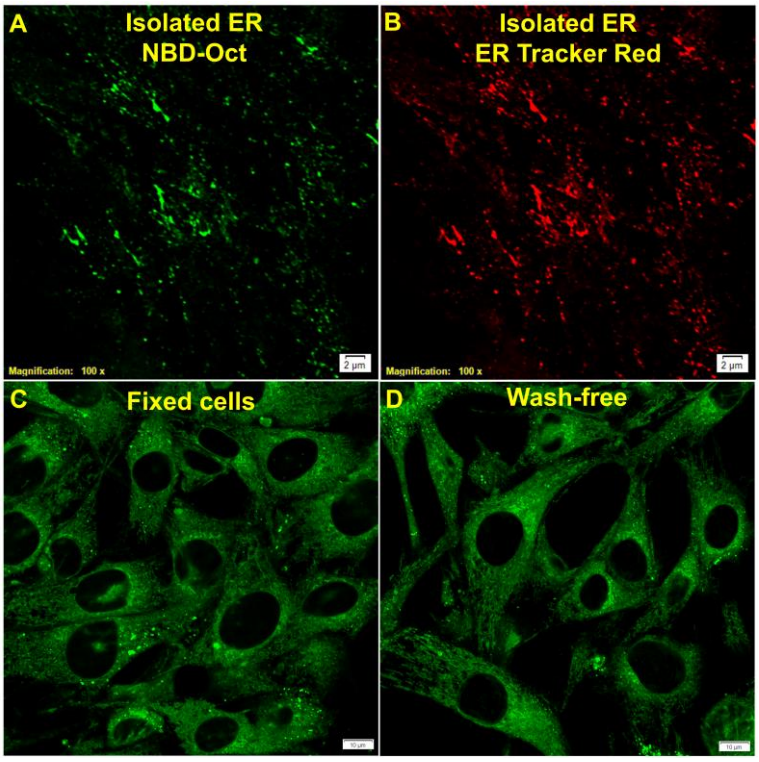

Figure 4. Isolated ER obtained by subcellular fractionation of live BHK-21 cells stained with (A) 2 μM **NBD-Oct** and (B) 0.3 μM ER Tracker Red (scale bar: 2 μm); (C) shows staining with **NBD-Oct** after formaldehyde fixation, and (D) shows a wash-free image of BHK-21 cells stained with **NBD-Oct** (scale bar: 10 μm).

with **NBD-Oct** and ER Tracker Red for 10 min. Finally, the solution was ultra-centrifuged again and the stained ER pellet was imaged under the confocal microscope. Much to our delight, the same fibrous microstructures were visualized in both green and red emission channels that indicated successful staining of the isolated ER using **NBD-Oct** (**Figure 4A-B**). The probe was also able to stain the ER in fixed cells as demonstrated in **Figure 4C**. The live BHK-21 cells were fixed using 4% paraformaldehyde followed by a 10-minute incubation with **NBD-Oct**. Moreover, the possibilities of wash-free imaging with this probe were also explored. The non-polar ER microenvironment compared to the bulk polarity of an aqueous medium suggested that the fluorescence turn-on behavior of the probe in a polar to the non-polar medium can be utilized for wash-free imaging. The probe accounts for zero background *i.e.*, the residual staining solution does not interfere with imaging and an excellent signal-to-noise ratio could be obtained even when no post-staining washing was performed (**Figure 4D**). Such wash-free property of the probe is advantageous for *in vivo* imaging applications.

2.5. Micropolarity inside ER in homeostatic and non-homeostatic conditions

Building upon the combined spectroscopic and microscopic results obtained until now, the probe **NBD-Oct** can be an ideal candidate to quantify the micropolarity inside ER. We anticipated ER micropolarity to act as a marker for ER stress − induced by the accumulation of misfolded and unfolded proteins which would play a role to affect the local environment of the ER. The impairment of protein glycosylation or disulfide-bond formation along with protein overexpression in the secretory pathway is considered to trigger ER stress.[26] The different stages of the cell cycle would also have an impact on such protein accumulation. Consequently, we have used **NBD-Oct** for monitoring ER micropolarity in homeostatic conditions, G_1/S, and G_2/M cell cycle arrest phases. For these experiments, we have taken four different cell lines − BHK-21, A549, MDA-MB-231, and HepG2. Initially, the cells were stained with 2 μM **NBD-Oct**, imaged, and spectral scanning in lambda mode was performed in a confocal laser scanning microscope (**Figure 5A-H**). For scanning, several regions of interest (ROI) were chosen for each case to have better confidence in the obtained dataset. The ER network gave completely different emission spectra as compared to the aqueous media. The emission spectrum of **NBD-Oct** in water was also recorded in the lambda scanning mode to maintain the same experimental condition for accurate comparison. In all four cell lines, significant blue shifts were observed while the ER in MDA-MB-231 showed the most non-polar environment (**Figure 5E-H**).

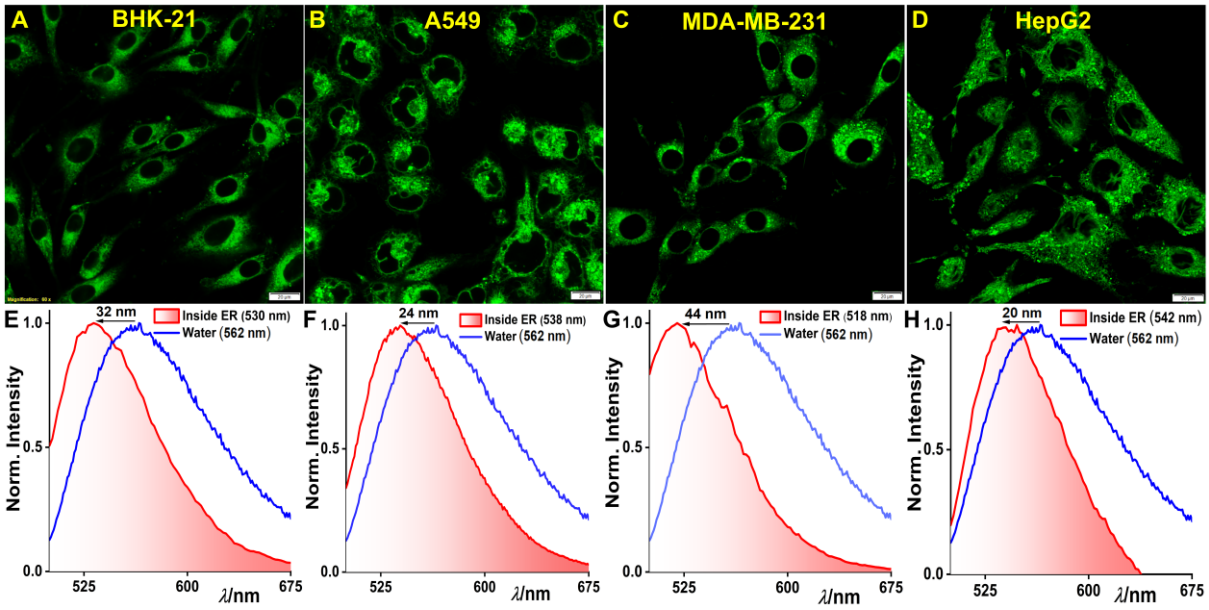

Figure 5. Micropolarity inside ER in homeostatic conditions. CLSM images of (A) BHK-21, (B) A549, (C) MDA-MB-231, and (D) HepG2 cells incubated with 2 μM **NBD-Oct**; (E), (F), (G), and (H) show the corresponding emission spectra recorded inside cells in lambda scanning mode (scale bar: 20 μm). The spectra recorded inside ER were compared with the bulk water spectra to understand the extent of the blue shift. The blue line denotes the spectra of **NBD-Oct** in water and the red line with a shaded area denotes spectra inside the ER [$\lambda_{ex}/\lambda_{em}$ = 488 nm/500 – 540 nm, laser power: 0.2 %, dwell time: 8 μs/pixel, confocal aperture: 1 AU; for lambda scanning: $\lambda_{ex}/\lambda_{em}$ = 488 nm/500 – 675 nm]

Moreover, the disparate nature of the emission spectra inside ER is indicative of the fact that ER microenvironment is unique to each cell line (**Table 1**). This finding suggests that **NBD-Oct** is capable of differentiating the ER microenvironment in different cell lines.

Now, following the ER micropolarity studies in homeostatic conditions, similar experiments were performed in different cell cycle arrest phases *i.e.*, G_1/S and G_2/M investigate if there was any change in the microenvironment. The same cell lines were exposed to the 24 h treatment with 100 ng.mL^{-1} tunicamycin − a well-known ER stress inducer that causes the activation of unfolded protein response (UPR). It eventually leads to the accumulation of cell cycle regulator protein p27 and G_1/S cell cycle arrest.[27] The spectral scanning experiment in the cells after G_1 arrest revealed substantial enhancement of ER micropolarity while MDA-MB-231 incurred the highest change with an 18 nm red-shifted spectrum (**Figure S19A-H**). Likewise, the DNA synthesis blocker molecule 5-fluorouracil (5-FU) was used as the inducer for G_2/M cell cycle arrest in those cell lines.[28] 5-FU is an antimetabolite drug that is widely used for the treatment of cancer. Following a 24 h treatment with 100 ng.mL^{-1} 5-FU, the cells were stained with **NBD-**

Oct, and spectral scanning was performed. Also in the G_2/M arrest phase, the spectra inside cells were found to be red-shifted as compared to the drug untreated cells (**Figure S20A-H**). Hence, it can be concluded that in both cell cycle arrest phases the micropolarity is higher than it was in the homeostatic condition possibly due to the accumulation of polar proteins.

Table 1. Emission properties of **NBD-Oct** inside the ER in different cells before and after arrests.

Cells	λ_{em}^{max} (nm) inside ER		
	Before arrest	After G_1 arrest	After G_2 arrest
BHK-21	530	540	545
A549	538	546	545
MDA-MB-231	518	536	534
HepG2	542	552	560

2.6. Imaging 3D tumoroids, *Caenorhabditis elegans*, and mice tissues

Optical microscopy has become an indispensable tool in contemporary biomedical research. The recent advancements in imaging techniques have significantly improved the choices available for *in vivo* imaging of animal research. Even though, the two-dimensional (2D) cell culture has been the most used research method, *in vivo* imaging provides compelling evidence suggesting that way more advanced experiments can be performed to come up with valuable insights. Hence, the applicability of the probe **NBD-Oct** as a versatile staining agent was further validated by imaging formaldehyde-fixed cells, three-dimensional (3D) spheroidal cell models, *Caenorhabditis elegans*, and animal tissue samples. Initially, we considered the 3D cell culture environment, known as 3D tumoroids or spheroids, which allows cells to grow and interact with the surrounding extracellular framework in three dimensions.[29] The tumoroid culture is a comparatively satisfactory model to mimic behavior and organization in terms of morphology and physiology. The spheroids were grown in a scaffold-free technique using live BHK-21 cells and treated with **NBD-Oct** for 10 mins. The confocal microscopy images indicate significant uptake of the probe by the tumoroids (**Figure 6A**), while the corresponding Z-scans show spherical morphologies of the individual cells grown in the cluster (**Figure S21**). The spheroid imaging experiments were followed by staining *Caenorhabditis elegans* which is the simplest and most frequently chosen model organism to study human diseases.[30] This model is regarded

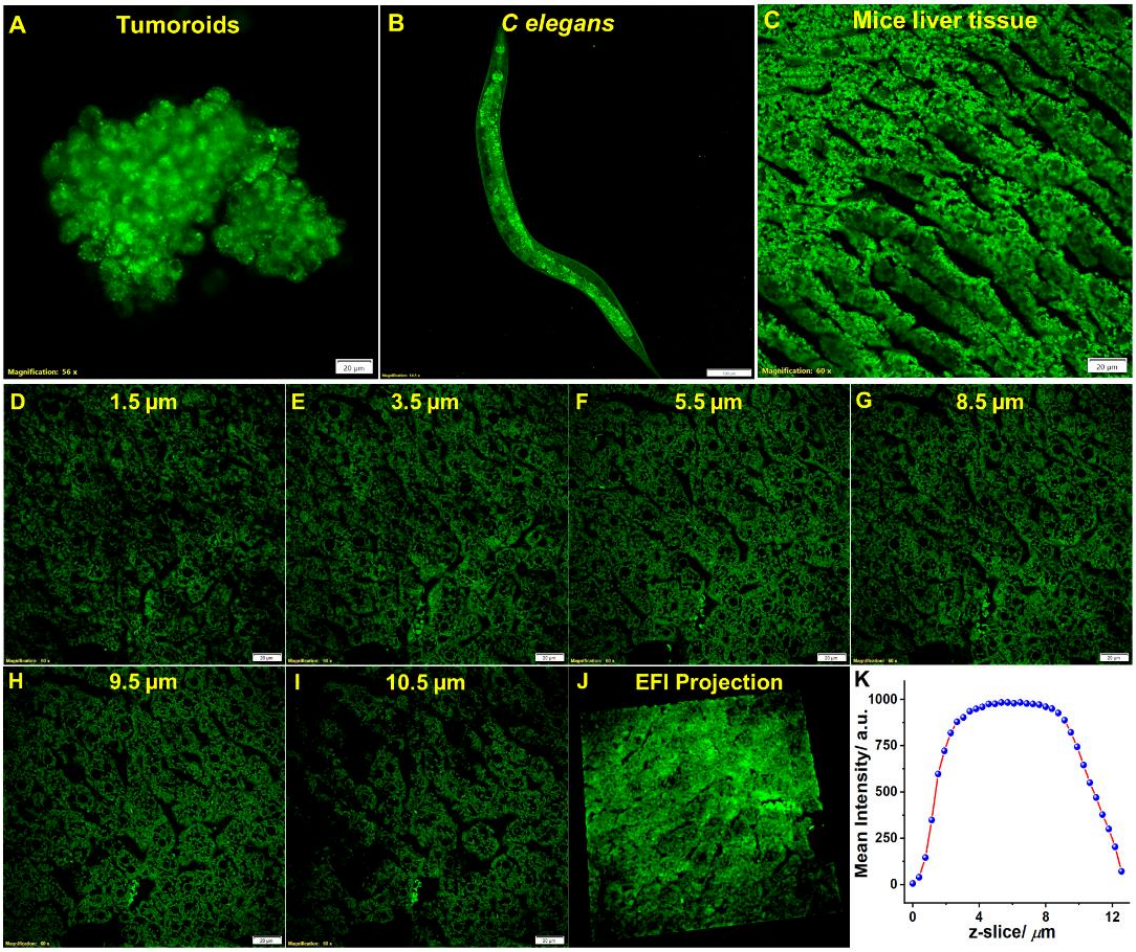

Figure 6. CLSM images of (A) 3D tumoroids, (B) *Caenorhabditis elegans*, and (C – J) wild-type mice liver tissues stained with 2 μM **NBD-Oct**; (D – I) show tissue section images at different z-depth, (J) shows the extended focus image (EFI) of the tissue section with enhanced SNR, and (K) shows the plot of mean intensity vs. z-slice as obtained from the tissue z-sectioning [$\lambda_{ex}/\lambda_{em}$ = 488 nm/500 – 540 nm, laser power: 0.2 %, dwell time: 8 μs/pixel, confocal aperture: 1 AU].

as a bridge between *in vitro* and *in vivo* models that provide physiologically relevant results being compliant with high-throughput technologies. Hence, for imaging, the wild-type N2 hermaphrodite worms were synchronized to the young adult stage and grown in the nematode growth media (NGM). The NGM itself contained 2 μM **NBD-Oct** and the worms were grown at 20°C for 60 h. The stained young adults were initially paralyzed by 5 mM levamisole treatment and then transferred to agar pads on glass slides. The confocal microscopy images show the whole tissue section is stained by the probe, rather than any specific region which corroborates with the reports suggesting the presence of a continuous ER lumen throughout the *Caenorhabditis elegans* structure (**Figure 6B**).[31] The beautifully stained worms indicated the

possibility of the probe for tissue imaging. Hence, to demonstrate further, wild-type mice liver tissue section was taken and incubated with the same probe concentration for 15 min. Next, we explored the applicability of the probe **NBD-Oct** to samples that may be difficult to image live such as human patient samples or large-number of mouse model samples. As a proof of concept, we used formalin-fixed wild-type mice liver tissue section and incubated with the same probe concentration for 15 min. As demonstrated in **Figure 6C-K**, this probe exhibits fast uptakability in the tissue sample and demonstrates applicability for large-scale animal and even human tissue imaging.

2.7. Communication between ER to Golgi Bodies

Alongside validating the versatility of **NBD-Oct** to image tumoroids, model organisms, and animal tissues, we took a specific interest to visualize the fate of the probe after cellular uptake in longer times. In our earlier experimental results, we demonstrated that **NBD-Oct** exclusively localizes in the endoplasmic reticulum of the cell. However, until this point, we did not have an idea of how long the probe is retained inside ER after localization. Even though probe retention was our subject of interest, another important biological phenomenon that we kept in our mind is ER to Golgi transport.[10] As the probe localizes in the ER driven by its hydrophobicity, there is every chance that it would bind to some ER protein and later get transported out of the ER lumen. Hence, we planned for two sets of experiments – co-staining with **NBD-Oct**/ER Tracker Red, **NBD-Oct**/BODIPY TR ceramide, subsequently, image them immediately and after 24 h. For the first set of experiments, the observation was – exclusive ER localization and very less Golgi localization, the corresponding Pearson's correlation coefficient values (PCC) being 0.94 and 0.43, respectively (**Figure 7A-D**, **7I-L**). The next set came up with exciting findings *i.e.*, while the ER localization was associated with a slightly lesser PCC value of 0.87 (**Figure 7E-H**), there was a massive enhancement in the Golgi localization indicated by a PCC value of 0.91 (**Figure 7M-P**). The same sets of experiments were performed in the HeLa cell line to further consolidate the obtained results in the normal cell line. In this case, too, we obtained a high PCC value of 0.88 for **NBD-Oct** vs. BODIPY TR ceramide after 24 h (**Figure S22**). Therefore, it can be concluded that **NBD-Oct**, alongside being a specific marker of ER, also enables the visualization of the ER to Golgi transport in the live cells. Once the probe was transported to the Golgi apparatus, we also performed lambda scanning and found that the Golgi environment is comparatively more polar that the ER (**Figure S23**). Now, these promising results led us to visualize the inhibition of ER to Golgi protein transport in live cells using

confocal microscopy. For this purpose, we have taken Brefeldin A (BFA) which blocks the transport of secreted and membrane proteins from the ER to the Golgi apparatus.[32] The live BHK-21 cells were stained with **NBD-Oct**/ BODIPY TR ceramide and followed by immediate treatment of 5 μM BFA for 24 h. The confocal images recorded thereafter did not show a good correlation between green/red channels, unlike BFA-untreated cells – the corresponding PCC value being 0.62 (**Figure S24**). However, it is possible to vary the extent of inhibition by changing the BFA concentration as well as the treatment time. Thus,

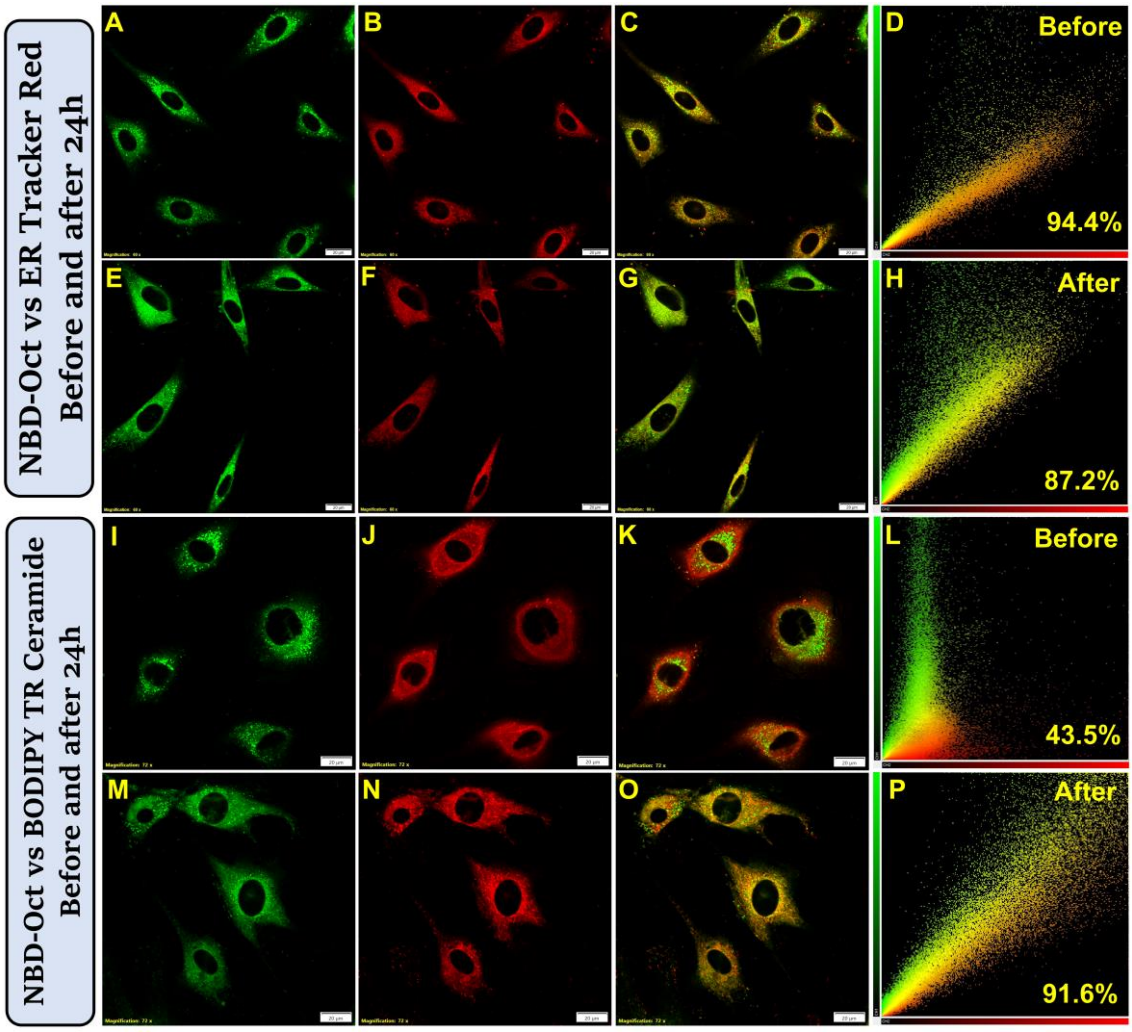

Figure 7. CLSM images show the transport from ER to Golgi in BHK-21 cells. The first and third rows show images taken immediately after 10 min staining. The second and fourth rows show images taken after 24 h of 10 min staining. Images (A, E, I, M) show cells stained with 2 μM **NBD-Oct**, (B, F) show cells stained with 0.3 μM ER Tracker Red, (J, N) show cells stained with BODIPY TR Ceramide; (C, G, K, O) are merge images, (D, H, L, P) are the corresponding scatter plots (scale bar = 20 μm) [$\lambda_{ex}/\lambda_{em}$ = 488 nm/500 – 540 nm, laser power: 0.2 %; $\lambda_{ex}/\lambda_{em}$ = 561 nm/575 – 620 nm, laser power: 0.5 %; dwell time: 8 μs/pixel, confocal aperture: 1 AU].

the effective trafficking inhibition in living cells by BFA treatment could be monitored by the straightforward microscopic approach. These findings are suggestive of studying inter-organelle communication between ER and Golgi using the developed probe.

3. Conclusion

This contribution introduces a series of biocompatible nitrobenzoxadiazole probes as wash-free markers of the endoplasmic reticulum in live cells. The probes diffused nicely in live cells with one of the probes, **NBD-Oct** exhibiting a diffusion coefficient value of 1.4 x 10^{-2} $\mu m^2.cm^{-1}$. Additionally, **NBD-Oct** showed efficient staining possibilities in isolated ER, 3D tumoroids, *Caenorhabditis elegans*, and mice tissue sections. The probe works on the principle of intramolecular charge transfer that enables the environment sensitivity based on the solvent polarity. We have taken advantage of this bulk polarity-sensitive behavior to quantitatively decipher the micropolarity changes in different cell cycle arrest phases. The study also shows that, even though cancer cells are more polar compared to normal cells, the ER micropolarity is unique for each cell line. The cell cycle arrests in G_1/S and G_2/M phases cause a significant increment in the ER micropolarity. Finally, the ER-Golgi transport in live cells has been visualized through optical microscopy using **NBD-Oct** as the staining agent. The long-term imaging revealed that Pearson's colocalization coefficient increases corresponding to the Golgi localization after 24 h of staining indicating the probe getting partitioned in both ER and Golgi. We believe, this probe alongside being cost-effective and easy to develop, comes up with a plethora of bioimaging applications and provides a quantitative idea of endoplasmic reticulum micropolarity and its response to induced stress.

4. Experimental Section/Methods

Materials and Methods: All the solvents and reagents were procured from commercial sources and used without any further purification. The spectroscopic grade solvents were purchased from Sisco Research Laboratories Pvt. Ltd. (SRL), India. 4-Chloro-7-nitrobenzofurazan (NBD-Cl) and $CDCl_3$ were purchased from Sigma Aldrich (USA). Butylamine, hexylamine, and octylamine were purchased from Alfa Aesar (USA). Dulbecco's Modified Eagle Medium (DMEM), L-Glutamine-Penicillin-Streptomycin solution (antibiotic cocktail), and Fetal Bovine Serum (FBS) were purchased from HiMedia (USA). Lyso-Tracker Red, MitoTracker Red, and ER Tracker Red were purchased from Thermo Fisher Scientific (USA). LipidSpot 610 was purchased from Biotium (USA). Brefeldin A was purchased from Sigma Aldrich (USA). 5-fluorouracil was purchased from Avra Synthesis Pvt. Ltd. (India). The spectroscopic

experiments in water were carried out using Milli-Q grade water using Milli-Q water purification set up from Merck (USA) with resistivity 18.2 MΩ•cm at 298 K. Thin layer chromatography (TLC) was performed using Merck Silica gel 60 F-254 pre-coated plates and visualized using UV-irradiation (λ = 254/365 nm). Silica gel from Merck (particle size 100-200 mesh) was used for column chromatography. ^{1}H and ^{13}C-NMR spectra were recorded on a Bruker 500 MHz spectrometer with operating frequencies of 126 MHz for ^{13}C. Chemical shifts (δ) are reported in ppm relative to the residual solvent signal (δ = 7.26 for ^{1}H NMR and δ = 77.0 for ^{13}C NMR). High-resolution mass spectrometry (HRMS) data were recorded on Bruker MicrOTOF-Q-II mass spectrometer using chloroform as the solvent. All absorption spectra and fluorescence measurements were carried out using SHIMADZU 1800 UV-Vis. spectrophotometer and HORIBA Jobin Yvon Fluorolog 3 equipped with a 450 W Xe arc lamp using 1 cm path length quartz cuvettes. Both excitation and emission slit widths were kept at 1 nm while recording the emission spectra. The absolute quantum yields in solution were measured using QuantaPhi integrating sphere luminescence yield system (HORIBA).

Cell Culture and Microscopy: BHK-21, A549, MDA-MB-231, HeLa, and HepG2 cells were obtained from National Center for Cell Science, and were grown in a 25 cm^2 cell culture flask in DMEM (phenol red free) containing 10% (v/v) FBS and 1% (v/v) antibiotic cocktail in 5% CO_2 at 37 °C in the incubator. For imaging purposes, cells were grown to 80% confluency in the 35 mm glass-bottom imaging dishes (170 ± 5 μm). The cells were co-incubated with 2 μM of the probe of interest and 0.3 μM of Lyso-Tracker Red / ER-Tracker Red / MitoTracker Red (whichever is applicable) for 10 minutes and washed with PBS (pH 7.4) twice before imaging. No washing step was performed in cases of incubation with alkylated NBD dyes only.
Tissue Sample Preparation: Wild-type liver tissues were collected from 10-to-14-week-old male mice. After collection, the tissues were paraffin-embedded and, subsequently, sectioned into 4 μm thick sections using a rotary microtome. Before staining, the paraffin-embedded sections were first (i) deparaffinized in xylene, (ii) rehydrated through graded ethanol washes, and (iii) rinsed twice with 1X PBS (pH 7.4).

ER Isolation: i) Cells were grown in a complete monolayer at high density. ii) The cells were scraped and taken in 1X PBS 7.4 (137 mM NaCl, 2.7 mM KCl, 10 mM Na_2HPO_4, 1.8 mM KH_2PO_4) on ice. iii) Sedimentation of cells @ 3000 rpm in swinging bucket rotor. iv) PBS was aspirated and 5 mM Hepes 7.4 was added. Any visible clumps were removed carefully. v) Cell lysis was performed by swelling the cells on ice. After 90% lysis, 5 mM $MgCl_2$, 100 mM KAc,

and 1X complete protease inhibitor were added. vi) The solution was fixed thoroughly and swung @ 3000 rpm to remove nuclei and non-lysed cells. vii) Further centrifugation of the supernatant was performed @ 12,000 rpm to pellet down mitochondria, lysosomes, and endosomes. viii) The pellets were removed and the supernatant was ultracentrifuged using MLA-80 tubes @ 70,000 for 1 h to obtain the ER pellet. ix) Finally, the pellet was put in membrane buffer (100 mM KAc, 50 mM HEPES, 5 mM $MgCl_2$, 250 mM sucrose), stained with the dye of interest, and imaged using a confocal microscope.

Confocal Microscopy: All the confocal microscopy imaging was performed with an Olympus FV3000 Confocal Laser Scanning Microscope (LSM). The image processing was done with the help of cellSens software (Olympus). For imaging, 488 nm (for alkylated NBD probes), 561 nm (ER/Lyso/Mito Tracker Red), and 594 nm (LipidSpot 610) excitation lasers were used. The confocal aperture was kept at 1.0 Airy Disk (AU) while the dwell time was maintained at 8 µs/pixel for all the imaging experiments. The laser power, gain, and offset were kept the same in all cases. The emission window was kept as 500 – 540 nm, 570 – 620 nm, and 600 – 640 nm for the excitation of 488 nm (0.5% of laser power), 561 nm (0.5% of laser power), and 594 nm respectively (1% of laser power). The images were acquired in sequential scan mode ensuring zero cross-talk between the imaging channels.

Synthesis of Alkylated-NBD Dyes: A solution of 4-Chloro-7-nitrobenzofurazan (NBD-Cl, 100 mg, 0.501 mmol) was prepared in 10 mL methanol. To that solution, 1.002 mmol of butylamine/ hexylamine/ octylamine was added dropwise followed by the addition of 20 μL triethylamine. Upon stirring at 298 K for 10 minutes, the color of the solution changed from pale yellow to dark brown and the progress of the reaction was checked by thin-layer chromatography. Then the solvent was removed under reduced pressure and the residue was purified by silica gel column chromatography using a 30 – 40% mixture of ethyl acetate and hexane as eluent and the yield was calculated ranging from 70% to 88% for different alkylated-NBD derivatives.

*N-butyl-7-nitrobenzo[c][1,2,5]oxadiazol-4-amine (**NBD-Bu**)*: ^{1}H NMR (Chloroform-*d*, 500 MHz) δ (ppm) 8.50 (d, J = 8.6 Hz, 1H), 6.21 (br. s, 1H), 6.18 (d, J = 8.6 Hz, 1H), 3.50 (q, J = 6.7 Hz, 2H), 1.86 – 1.75 (m, 3H), 1.56 – 1.46 (m, 2H), 1.02 (t, J = 7.3 Hz, 3H). ^{13}C NMR (Chloroform-*d*, 125 MHz) δ (ppm) 144.26, 143.88, 136.50, 123.98, 98.49, 43.71, 30.54, 20.14, 13.67. HRMS (ESI) *m*/*z*: $[M + Na]^+$ calcd for $C_{10}H_{12}N_4O_3$ 236.0909; found, 236.0982.

N-hexyl-7-nitrobenzo[c][1,2,5]oxadiazol-4-amine ***(NBD-Hex)***: Yield = 79%. ^{1}H NMR (Chloroform-*d*, 500 MHz) δ (ppm) 8.50 (d, J = 8.6 Hz, 1H), 6.21 (br. s, 1H), 6.17 (d, J = 8.6 Hz, 1H), 3.49 (q, J = 6.8 Hz, 2H), 1.85 – 1.78 (m, 2H), 1.52 – 1.44 (m, 2H), 1.40 – 1.33 (m, 4H), 0.92 (t, J = 7.0 Hz, 3H). ^{13}C NMR (Chloroform-*d*, 125 MHz) δ (ppm) 144.27, 143.89, 143.82, 136.47, 124.05, 98.48, 44.00, 31.36, 28.53, 26.62, 22.51, 13.97. HRMS (ESI) *m*/*z*: $[M + Na]^+$ calcd for $C_{12}H_{16}N_4O_3$ 287.1119; found, 287.1115.

N-octyl-7-nitrobenzo[c][1,2,5]oxadiazol-4-amine ***(NBD-Oct)***: Yield = 88%. ^{1}H NMR (Chloroform-*d*, 500 MHz) δ (ppm) 8.50 (d, J = 8.6 Hz, 1H), 6.20 (br. s, 1H), 6.17 (d, J = 8.6 Hz, 1H), 3.52 – 3.45 (q, 2H), 1.86 – 1.77 (m, 2H), 1.51 – 1.44 (m, 2H), 1.40 – 1.27 (m, 8H), 0.88 (t, J = 7.0 Hz, 2H). ^{13}C NMR (Chloroform-*d*, 125 MHz) δ (ppm) 144.41, 144.04, 143.99, 136.63, 124.14, 98.63, 44.15, 31.87, 29.31, 29.26, 28.69, 27.09, 22.75, 14.21. HRMS (ESI) *m*/*z*: $[M + Na]^+$ calcd for $C_{14}H_{20}N_4O_3$ 315.1432; found, 315.1428.

Acknowledgments

We thank the Department of Chemistry and Central Instrumentation Facility at the Indian Institute of Science Education and Research Bhopal (IISERB) for the instrumentation and infrastructural facility. TD thanks IISERB for his doctoral fellowship. We also thank Dr. Ishaan Gupta (IIT Delhi) for his suggestions. We acknowledge the Department of Science and Technology (DST), India, for the FIST support (SR/FST/LSI-643/2015) for the live-cell imaging facility. We also thank Dr. Yogesh Hooda (University of Cambridge, UK) for helping with the microsome separation protocol.

Conflict of Interest

A provisional Indian patent application has been submitted.

Data Availability Statement

The data that support the findings of this study are available from the corresponding author upon reasonable request.

References

[1] a) D. S. Schwarz, M. D. Blower, *Cell. Mol. Life Sci.* **2016**, *73*, 79-94; b) L. M. Westrate, J. E. Lee, W. A. Prinz, G. K. Voeltz, *Annu. Rev. Biochem.* **2015**, *84*, 791-811; c) F. J. Stevens, Y. Argon, *Semin. Cell Dev. Biol.* **1999**, *10*, 443-454.

[2] L. Ellgaard, N. McCaul, A. Chatsisvili, I. Braakman, *Traffic* **2016**, *17*, 615-638.

[3] a) M. Csala, G. Banhegyi, A. Benedetti, *FEBS Lett.* **2006**, *580*, 2160-2165; b) D. Mekahli, G. Bultynck, J. B. Parys, H. De Smedt, L. Missiaen, *Cold Spring Harb. Perspect. Biol.* **2011**, *3*, 1-32; c) J. Rieusset, *Biochim. Biophys. Acta - Mol. Cell Res.* **2017**, *1864*, 865-876.

[4] M. Puhka, H. Vihinen, M. Joensuu, E. Jokitalo, *J. Cell Biol.* **2007**, *179*, 895-909.

[5] C. Vedrenne, H. P. Hauri, *Traffic* **2006**, *7*, 639-646.

[6] K. Vermeulen, D. R. Van Bockstaele, Z. N. Berneman, *Cell Prolif.* **2003**, *36*, 131-149.

[7] a) K. Bourougaa, N. Naski, C. Boularan, C. Mlynarczyk, M. M. Candeias, S. Marullo, R. Fahraeus, *Mol. Cell* **2010**, *38*, 78-88; b) C. Han, L. Jin, Y. Mei, M. Wu, *Cell Signal* **2013**, *25*, 144-149; c) N. Song, Y. Song, B. Hu, X. Liu, X. Yu, H. Zhou, J. Long, Z. Yu, *Adv. Healthcare Mater.* **2022**, *n/a*, 2202039; d) Y. Li, X. Zhang, X. Wan, X. Liu, W. Pan, N. Li, B. Tang, *Adv. Funct. Mater.* **2020**, *30*, 2000532.

[8] a) C. Hetz, E. Chevet, H. P. Harding, *Nat. Rev. Drug Discov.* **2013**, *12*, 703-719; b) S. Y. Wang, R. J. Kaufman, *J. Cell Biol.* **2012**, *197*, 857-867; c) M. Wang, R. J. Kaufman, *Nature* **2016**, *529*, 326-335; d) H. Yoshida, *FEBS J.* **2007**, *274*, 630-658.

[9] a) T. Dutta, K. Pal, A. L. Koner, *Chem. Rec.* **2022**, e202200035; b) K. Pal, T. Dutta, A. L. Koner, *ACS Omega* **2021**, *6*, 28-37; c) W. Xu, Z. B. Zeng, J. H. Jiang, Y. T. Chang, L. Yuan, *Angew. Chem. Int. Ed.* **2016**, *55*, 13658-13699.

[10] a) P. Watson, D. J. Stephens, *Biochim. Biophys. Acta Mol. Cell Res.* **2005**, *1744*, 304-315; b) J. McCaughey, D. J. Stephens, *Trends Cell Biol.* **2019**, *29*, 940-953.

[11] D. Tang, Y. Wang, *Trends Cell Biol.* **2013**, *23*, 296-304.

[12] N. Gomez-Navarro, E. Miller, *J. Cell Biol.* **2016**, *215*, 769-778.

[13] a) Y. Suda, K. Kurokawa, A. Nakano, *Front. Cell Dev. Biol.* **2018**, *5*, 1-6; b) P. T. A. Linders, C. van der Horst, M. ter Beest, G. van den Bogaart, *Cells* **2019**, *8*; c) E. C. Gaynor, T. R. Graham, S. D. Emr, *Biochim. Biophys. Acta Mol. Cell Res.* **1998**, *1404*, 33-51.

[14] a) W. Shu, S. P. Zang, C. Wang, M. X. Gao, J. Jing, X. L. Zhang, *Anal. Chem.* **2020**, *92*, 9982-9988; b) S. J. Park, V. Juvekar, J. H. Jo, H. M. Kim, *Chem. Sci.* **2020**, *11*, 596-601; c) K. Pal, I. Samanta, R. K. Gupta, D. Goswami, A. L. Koner, *Chem. Commun.* **2018**, *54*, 10590-10593.

[15] a) J. Y. Wu, A. Y. Bi, F. Zheng, S. Huang, Y. J. Li, J. P. Ding, D. X. Xiang, W. B. Zeng, *Chem. Commun.* **2021**, *57*, 801-804; b) L. Hu, B. S. Xu, H. Chen, H. Wang, *Sens. Actuators B Chem.* **2021**, *340*, 129950; c) H. R. Jia, Y. X. Zhu, K. F. Xu, G. Y. Pan, X. Y. Liu, Y. Qiao, F. G. Wu, *Chem. Sci.* **2019**, *10*, 4062-4068.

[16] a) W. H. Song, B. L. Dong, Y. R. Lu, X. Q. Kong, A. H. Mehmood, W. Y. Lin, *New J. Chem.* **2019**, *43*, 12103-12108; b) H. B. Xiao, P. Li, B. Tang, *Coord. Chem. Rev.* **2021**,

427; c) J. Yin, W. Quan, X. Kong, C. Liu, B. Lu, W. Lin, *ACS Appl. Bio Mater.* **2021**, *4*, 3630-3638; d) Q. Q. Bai, C. J. Yang, M. J. Yang, Z. Q. Pei, X. B. Zhou, J. X. Liu, H. W. Ji, G. Li, M. M. Wu, Y. L. Qin, Q. Wang, L. Wu, *Anal. Chem.* **2022**, *94*, 2901-2911; e) P. Alam, W. He, N. L. C. Leung, C. Ma, R. T. K. Kwok, J. W. Y. Lam, H. H. Y. Sung, I. D. Williams, K. S. Wong, B. Z. Tang, *Adv. Funct. Mater.* **2020**, *30*, 1909268.

[17] a) C. Y. Jiang, H. J. Huang, X. Y. Kang, L. Yang, Z. Xi, H. Y. Sun, M. D. Pluth, L. Yi, *Chem. Soc. Rev.* **2021**, *50*, 7436-7495; bT. Yamaguchi, M. Asanuma, S. Nakanishi, Y. Saito, M. Okazaki, K. Dodo, M. Sodeoka, *Chem. Sci.* **2014**, *5*, 1021-1029.

[18] a) S. K. Das, A. S. Patra, D. Jose, M. Sarkar, *Chem. Phys. Lett.* **2012**, *528*, 11-15; b) W. Q. Chen, H. C. Luo, X. J. Liu, J. W. Foley, X. Z. Song, *Anal. Chem.* **2016**, *88*, 3638-3646; c) N. C. P. Araujo, R. Afonso, A. Bringela, M. L. Cancela, M. L. S. Cristiano, R. B. Leite, *Parasitol. Int.* **2013**, *62*, 575-582.

[19] a) L. F. Guo, C. Y. Li, H. Shang, R. Y. Zhang, X. C. Li, Q. Lu, X. Cheng, Z. Q. Liu, J. Z. Sun, X. Q. Yu, *Chem. Sci.* **2020**, *11*, 661-670; b) R. Yang, F. F. Meng, G. L. Niu, J. Niu, Q. H. Hao, C. Zong, P. Gao, X. Q. Yu, *Sens. Actuators B Chem.* **2022**, *372*, 132639.

[20] T. Sander, J. Freyss, M. von Korff, C. Rufener, *J. Chem. Inf. Model* **2015**, *55*, 460-473.

[21] a) Z. Yang, Y. He, J. H. Lee, W. S. Chae, W. X. Ren, J. H. Lee, C. Kang, J. S. Kim, *Chem. Commun.* **2014**, *50*, 11672-11675; b) H. Lee, Z. Yang, Y. Wi, T. W. Kim, P. Verwilst, Y. H. Lee, G. I. Han, C. Kang, J. S. Kim, *Bioconjugate Chem.* **2015**, *26*, 2474-2480.

[22] A. P. Demchenko, *Methods Appl. Fluoresc.* **2020**, *8*, 022001.

[23] a) E. A. J. Reits, J. J. Neefjes, *Nat. Cell Biol.* **2001**, *3*, E145-E147; b) A. Kitamura, M. Kinjo, *Biophys Physicobiol* **2018**, *15*, 1-7.

[24] M. Kang, C. A. Day, A. K. Kenworthy, E. DiBenedetto, *Traffic* **2012**, *13*, 1589-1600.

[25] a) J. B. Harford, J. S. Bonifacino, *Curr. Protoc. Cell Biol.* **2011**, *52*, 3.0.1-3.0.8; b) B. Alberts, Johnson, A., Lewis, J., Raff, M., Roberts, K. and Walter, P., *Molecular biology of the cell, 4th Ed.*, 4th ed. ed., Garland Science, **2002**.

[26] N. Cherepanova, S. Shrimal, R. Gilmore, *Curr. Opin. Cell Biol.* **2016**, *41*, 57-65.

[27] B. Durand, F. B. Gao, M. Raff, *EMBO J.* **1997**, *16*, 306-317.

[28] R. Yoshikawa, M. Kusunoki, H. Yanagi, M. Noda, J. I. Furuyama, T. Yamamura, T. Hashimoto-Tamaoki, *Cancer Res.* **2001**, *61*, 1029-1037.

[29] a) S. A. Langhans, *Front. Pharmacol.* **2018**, *9*, 1-14; b) N. E. Ryu, S. H. Lee, H. Park, *Cells* **2019**, *8*, 1-13.

[30] a) P. M. Meneely, C. L. Dahlberg, J. K. Rose, *Curr. Protoc. Essent. Lab. Tech.* **2019**, *19*, 1-35; b) M. B. Veldman, S. Lin, *Pediatr. Res.* **2008**, *64*, 470-476; c)T. Kaletta, M. O. Hengartner, *Nat. Rev. Drug Discov.* **2006**, *5*, 387-398.

[31] Z. Y. Lee, M. Prouteau, M. Gotta, Y. Barral, *J. Cell Biol.* **2016**, *214*, 665-676.

[32] a) A. Colanzi, G. Grimaldi, G. Catara, C. Valente, C. Cericola, P. Liberali, M. Ronci, V. S. Lalioti, A. Bruno, A. R. Beccari, A. Urbani, A. De Flora, M. Nardini, M. Bolognesi, A. Luini, D. Corda, *Proc. Natl. Acad. Sci. USA* **2013**, *110*, 9794-9799; b) T. Fujiwara, K. Oda, S. Yokota, A. Takatsuki, Y. Ikehara, *J. Biol. Chem.* **1988**, *263*, 18545-18552.